ACS APPLIED MATERIALS & INTERFACES

Research Article

www.acsami.org

Oxygen Vacancy Induced Room Temperature Ferromagnetism in Pr-Doped CeO_2 Thin Films on Silicon

Gang Niu,*[,†] Erwin Hildebrandt,[‡] Markus Andreas Schubert,[†] Federico Boscherini,[§] Marvin Hartwig Zoellner,[†] Lambert Alff,[‡] Damian Walczyk,[†] Peter Zaumseil,[†] Ioan Costina,[†] Henrik Wilkens,[∥] and Thomas Schroeder[†,⊥]

[†]IHP, Im Technologiepark 25, 15236 Frankfurt (Oder), Germany

[‡]Institute of Materials Science, Technische Universität Darmstadt, 64287 Darmstadt, Germany

[§]Department of Physics and Astronomy and CNISM, University of Bologna, Viale C. Berti Pichat 6/2, 40127 Bologna, Italy

[∥]Fachbereich Physik, Universität Osnabrück, Barbarastraße 7, D-49069 Osnabrück, Germany

[⊥]BTU Cottbus-Senftenberg, Konrad-Zuse-Straße 1, 03046 Cottbus, Germany

Supporting Information

ABSTRACT: Integration of functional oxides on Si substrates could open a pathway to integrate diverse devices on Si-based technology. Oxygen vacancies ($Vo^{\cdot\cdot}$) can strongly affect solid state properties of oxides, including the room temperature ferromagnetism (RTFM) in diluted magnetic oxides. Here, we report a systematical study on the RTFM of oxygen vacancy engineered (by Pr^{3+} doping) CeO_2 epitaxial thin films on Si substrates. High quality, mixed single crystalline $Ce_{1-x}Pr_xO_{2-\delta}$ ($x = 0-1$) solid solution films were obtained. The Ce ions in CeO_2 with a fluorite structure show a Ce^{4+}-dominant valence state in all films. The local crystal structures of the films were analyzed in detail. Pr doping creates both $Vo^{\cdot\cdot}$ and PrO_8-complex defects in CeO_2 and their relative concentrations vary with the Pr-doping level. The RTFM properties of the films reveal a strong dependence on the relative $Vo^{\cdot\cdot}$ concentration. The RTFM in the films initially increases with higher Pr-doping levels due to the increase of the F^+ center ($Vo^{\cdot\cdot}$ with one occupied electron) concentration and completely disappears when $x > 0.2$, where the magnetic polaron concentration is considered to decline below the percolation threshold, thus long-range FM order can no longer be established. We thus demonstrate the possibility to directly grow RTFM Pr-doped CeO_2 films on Si substrates, which can be an interesting candidate for potential magneto-optic or spintronic device applications.

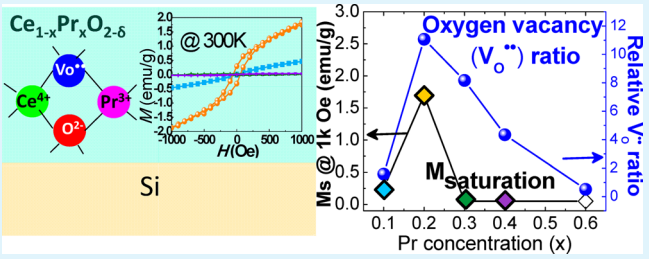

KEYWORDS: *ferromagnetism, oxides, thin films, oxygen vacancies, doping*

1. INTRODUCTION

The growth of functional (e.g., ferroelectric, ferromagnetic, etc.) crystalline oxides on Si has attracted much interest in recent years[1,2] because it opens a pathway to monolithically integrate various devices, such as nonvolatile memories,[3,4] micro-electro-mechanical systems (MEMS),[5] modulators,[6] spintronic devices,[7] etc., with mainstream semiconductor technology. Ceria (CeO_2), which possesses a high dielectric constant ($\varepsilon = 26$) and rather small lattice mismatch with respect to Si (−0.4%), has initially drawn much attention as a possible high-κ dielectric candidate[8] and as a buffer for other functional (e.g., superconductive) oxides.[9] Furthermore, thanks to its exceptional oxygen storage capability, CeO_2 is also well-studied for other applications like catalysis,[10] fuel cells,[11] oxygen sensors,[12] etc. More recently, it is reported that doped and/or pure CeO_2 can be ferromagnetic at room temperature.[13−18]

Many oxides such as ZnO,[19] TiO_2,[20] In_2O_3,[21] Al_2O_3,[22] HfO_2,[23,24] CeO_2, etc. show room temperature ferromagnetism (RTFM) in their nanoparticle form or when doped with a small amount of metals. These oxides are known as diluted magnetic oxides (DMO) and the exploration of RTFM in DMO is at the forefront of FM material research because its exchange mechanism is expected to differ from our traditional understanding of FM. Although the origin of RTFM in DMO is still under controversy, defects, particularly oxygen vacancies ($Vo^{\cdot\cdot}$) in oxides, appear to play a critical role. Coey et al. proposed a widely accepted model, the F-center exchange mechanism, according to which an electron trapped in an F-center (i.e., $Vo^{\cdot\cdot}$) can act as a coupling agent between magnetic ions, thus invoking long-ranged FM ordering.[25]

Doping with metals of lower valence states is an effective way to induce $Vo^{\cdot\cdot}$ in CeO_2. Intensive studies have been focused on the 3*d* transition metals (TM, e.g., Ni^{2+},[26] Co^{2+},[27−29] Cr^{2+},[30]

Received: April 13, 2014
Accepted: September 25, 2014
Published: September 25, 2014

Cu^{2+},[31] Fe^{2+},[32] etc.)-doped CeO_2 and the F-center model was applied to explain observed RTFM in these systems. However, it is suggested that problems of the secondary metallic phase can usually exist in TM-doped oxides, i.e., TM doping ions probably do not incorporate into the oxide lattices but phase segregate into TM oxide nanoparticles, which would contribute to the total FM at certain particles sizes.[29,33] This argument may thus weaken or deny the correlation between RTFM and $Vo^{\cdot\cdot}$. Such problems could be overcome in rare earth (RE)-doped CeO_2, in which RE ions in CeO_2 lead to solid solutions in the form of $Ce_{1-x}RE_xO_{2-\delta}$.[17,34,35] However, few results on FM behavior of RE-doped CeO_2 have been reported and most of them deal with polycrystalline oxide powders.[17,36,37]

In this work, we grow high quality, single crystalline Pr-doped CeO_2 epitaxial films with a systematic stoichiometry variation on Si(111) substrates and investigate their FM characteristics at room temperature. While CeO_2 adopts a cubic fluorite structure ($Fm\bar{3}m$) with Ce showing a +4 valence state, its neighboring RE oxide praseodymium oxide, which has a complex phase diagram,[38] shows a clear preference for the Pr^{3+} valence state either in the form of a cubic bixbyite ($Ia\bar{3}$) or hexagonal ($P\bar{3}m1$) structure. Bixbyite can be considered as an intrinsic oxygen deficient fluorite in which the lattice parameter is doubled by removing in a systematic way a quarter of the oxygen atoms.[39,40] We will show that real mixed $Ce_{1-x}Pr_xO_{2-\delta}$ ($x = 0-1$) solid solution films have been obtained and doping Pr^{3+} into CeO_2 lattice can effectively create $Vo^{\cdot\cdot}$ in CeO_2 films. It will also be demonstrated that FM properties dramatically depend on the Pr-doping level (thus relative $Vo^{\cdot\cdot}$ concentration) in the films. The $Ce_{0.8}Pr_{0.2}O_{2-\delta}$ film shows an optimal relative $Vo^{\cdot\cdot}$ concentration and remarkable RTFM behavior with a saturation magnetization $M_s \sim 1.8$ emu/g. Our results help to better understand the correlation between $Vo^{\cdot\cdot}$ and RTFM in oxides and demonstrate the possibility of directly growing RTFM oxide thin films on Si for magneto-optic or spintronic device applications.

2. EXPERIMENTAL SECTION

2.1. Film Growth. All the $Ce_{1-x}Pr_xO_{2-\delta}$ samples were fabricated by an electron beam coevaporation method using a molecular beam epitaxy (MBE) DCA 600 reactor. Prior to the introduction into the ultrahigh vacuum (UHV) chamber (base pressure $\sim 10^{-10}$ mbar), 4 in. *p*-Type Si(111) ($\rho = 5-15\ \Omega$) wafers were first cleaned by a standard HF-etching procedure to form an H-terminated surface.[41] An annealing at 750 °C for 10 min under UHV was subsequently performed to prepare high-quality (7 × 7) reconstructed surfaces (see Figure S1, Supporting Information). The growth temperature was 625 °C and the typical O_2 partial pressure during the growth was 2×10^{-6} mbar. A ~2 nm Pr_2O_3 passivation layer was grown before the coevaporation in order to protect the Si surface from oxidizing at the very beginning of the growth, thus ensuring high-quality films.[42] The crystallinity of the films was in situ monitored by reflection high-energy electron diffraction (RHEED). $Ce_{1-x}Pr_xO_{2-\delta}$ films with different Pr-doping levels of $x = 0.1$, 0.2, 0.3, 0.4, and 0.6 were grown and pure CeO_2 and Pr_2O_3 films were also fabricated as references. A postdeposition annealing (PDA) at 400 °C under $P_{O_2} = 1$ bar was performed for all the samples in order to avoid any hexagonal Pr_2O_3 phase.[43]

2.2. Characterization. The valence states of elements were ex situ analyzed using an X-ray photoelectron spectroscopy (XPS) chamber equipped with a Mg Kα X-ray source ($E_{excitation} = 1253.6$ eV) and the stoichiometries were also determined by quantitative XPS analysis by calculating the XPS peak areas below the curves. More details can be found in ref 44.

Two X-ray diffraction (XRD) apparatus with different arrangements were used to detect the crystalline quality of the samples: a Rigaku DMAX 1500 (Cu Kα radiation) in a medium-resolution setup without a crystal monochromator and a Rigaku SmartLab diffractometer (Cu Kα_1 radiation, $\lambda = 1.5406$ Å) in a high-resolution setup with a Ge (400) ×2 crystal collimator. High-resolution transmission electron microscopy (HRTEM) measurements were performed using a FEI Tecnai Osiris machine operated at 200 kV. Samples for TEM were prepared conventionally by grinding, polishing, and Argon ion milling. X-ray reflectivity (XRR) was used to determine oxide film thicknesses, and the typical film thickness was ~24 nm. Thicker samples of ~87 nm were fabricated for synchrotron-based X-ray absorption near edge structure spectroscopy (XANES), which provides information on the oxidation state and local coordination chemistry of Ce/Pr atoms. The XANES measurements on films were performed in fluorescence mode using the XAFS beamline of ELETTRA synchrotron center in Trieste, Italy. Raman spectra of the samples were detected at room temperature by a Renishaw inVia spectrometer with an unpolarized He−Cd ultraviolet (UV) laser line ($\lambda = 325$ nm) as an excitation source and a backscattering configuration. Magnetization measurements have been performed using a magnetic property measurement system (MPMS) utilizing a superconducting quantum interference device (SQUID) from Quantum Design. Data has been obtained at 300 K. To ensure full saturation magnetization, H was set to ±50 kOe during hysteresis measurements.

3. RESULTS AND DISCUSSION

3.1. Single Crystalline Solid Solution $Ce_{1-x}Pr_xO_{2-\delta}$ Films. Specular θ-2θ X-ray diffraction (XRD) measurements were performed to characterize the crystalline quality of the epitaxial $Ce_{1-x}Pr_xO_{2-\delta}$ films, as shown in Figure 1. For all the samples, a sharp, intense Si(222) Bragg peak arises at $2\theta = 58.88°$. It is noted that the samples of $x = 0-0.2$ were characterized by a medium-resolution diffractometer (DMAX 1500), thus their Si(222) peaks show a double-peak feature related to Cu Kα_1 and Cu Kα_2 (222) reflections. For samples of $x = 0.3-0.6$, only Cu Kα_1 reflection can be observed for the Si(222) peak, thanks to the utilization of a high-resolution diffractometer (Rigaku SmartLab) equipped with a crystal monochromator. In addition to the Si reflection, all the films demonstrate only one peak corresponding to the oxide. The

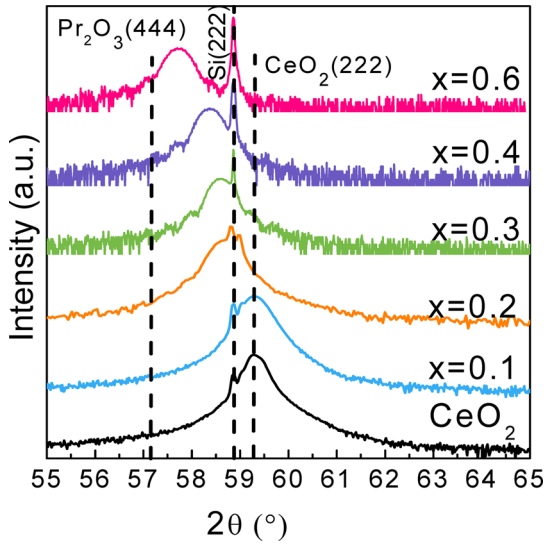

Figure 1. XRD specular θ-2θ measurements of $Ce_{1-x}Pr_xO_{2-\delta}$ films with $x = 0$, 0.1, 0.2, 0.3, 0.4, and 0.6. The peak positions of Si(222), Pr_2O_3(444), and CeO_2(444) are marked by dotted lines.

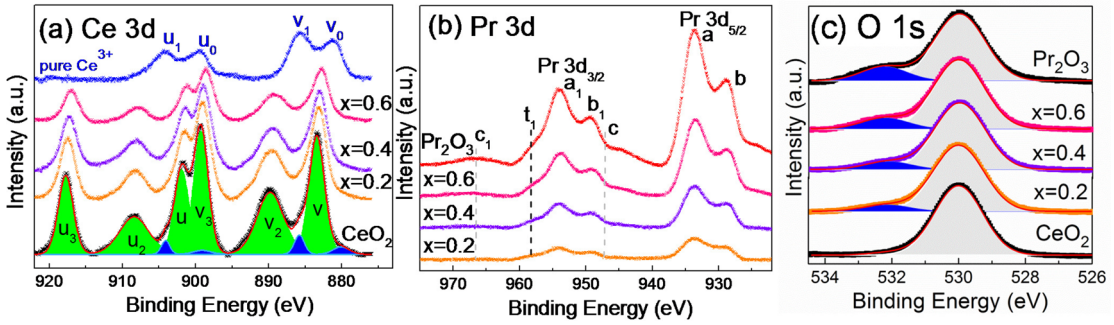

Figure 2. XPS spectra after subtracting a Shirley background for $Ce_{1-x}Pr_xO_{2-\delta}$ films (x = 0, 0.2, 0.4, 0.6, and 1): (a) Ce 3d spectra with a pure Ce_2O_3 reference (blue curve) and the deconvolution of pure CeO_2 spectrum is shown; (b) Pr 3d spectra with a Pr_2O_3 reference (red curve); (c) O 1s spectra with fittings.

oxide spectra measured by a high-resolution diffractometer display thickness-related interference fringes at the foot of the main oxide peak, thus revealing a sharp interface structure between epitaxial films and Si. Furthermore, the oxide peaks are symmetric, unsplit, and their positions shift from the pure CeO_2(222) position (2θ = 59.28°, marked by dotted line) to cubic Pr_2O_3(444) (2θ = 57.21°, marked by dotted line) with the increase of the Pr-doping level. This indicates that real mixed solid solutions were formed and with the increase of Pr concentration the lattice parameter of the mixed film becomes larger. For the metal-doped FM oxides, a significant question to answer is whether there exists metal ion phase separation that impacts FM properties.[45] XRD results over a wide 2θ range (see Figure S2, Supporting Information and more details in ref 49) reveal that no extra diffractions from metal cluster impurities or other oxide phases were detected and the Pr dopant atoms are completely incorporated into the CeO_2 lattice. A similar phenomenon was observed in other RE mixed oxides such as $(Pr,Y)_2O_3$[46] or $(La,Lu)_2O_3$,[47] in which the stoichiometries can be precisely determined with extracted lattice parameters by using Vegard's law.[48] In the case of the Ce–Pr mixture, despite the possible presence of Pr^{4+}, which can influence the calculation,[43] the stoichiometries estimated using Vegard's law are also roughly consistent with those estimated by quantitative X-ray photoelectron spectroscopy (XPS).

3.2. Valence States of Ce and Pr. Figure 2a–c shows the ex situ XPS spectra after subtracting a Shirley background of Ce 3d, Pr 3d, and O 1s, respectively, for $Ce_{1-x}Pr_xO_{2-\delta}$ samples with x = 0.2, 0.4, and 0.6. A detailed in situ XPS study on the as-grown samples without breaking the ultrahigh vacuum (UHV) ambiance has been reported in our prior study (ref 49), which pointed out that Pr^{3+} doping into CeO_2 films affects the Ce ions valence state and higher Pr concentration results in more Ce^{3+} in the films. In particular, the $Ce_{0.2}Pr_{0.8}O_{2-\delta}$ film contains only Ce^{3+} ion. Compared to in situ results, ex situ Ce 3d XPS spectra shown in Figure 2a demonstrate an entirely different behavior. Although the signal intensity decreases along with the increasing Pr concentration, all the mixture samples show a completely similar spectrum shape as the nondoped CeO_2 film (black curve). A spectrum of pure Ce^{3+} (blue curve) is given for comparison. This result indicates that original Ce^{3+} ions in UHV samples were further oxidized after exposure to air due to the exceptional oxygen storage property of CeO_2 and all the samples show the Ce^{4+} dominant feature not being influenced by Pr doping. More information can be obtained by fitting the spectra. The Ce 3d spectrum of CeO_2 was fitted using the Gaussian–Lorentzian profile, the deconvolution of which presents three intense spin–orbit doublets (u/v, u_2/v_2, and u_3/v_3, green peaks) and two much weaker ones (u_0/v_0 and u_1/v_1, blue peaks), referring to Ce^{4+} and Ce^{3+} final states, respectively.[50,51] The u-series and v-series peaks represent Ce $3d_{3/2}$ and $3d_{5/2}$ states, respectively. The relative Ce^{3+} concentration in the films can be determined by $[Ce^{3+}]/[Ce^{3+} + Ce^{4+}] = (A_{u0} + A_{v0} + A_{u1} + A_{v1})/(A_{u0} + A_{v0} + A_{u1} + A_{v1} + A_u + A_v + A_{u2} + A_{v2} + A_{u3} + A_{v3})$, where $A_u(A_v)$ are the spectral peak areas.[52] The estimated Ce^{3+} concentration is a constant of ~5.4% for all the films including the pure CeO_2 film. We attribute this phenomenon to the surface reduction of CeO_2 due to the UHV characteristics of the XPS technique, namely, CeO_2 probably loses oxygen to a certain degree near the film surface in the UHV environment.[53,54]

Figure 2b presents Pr 3d spectra. Besides the intensity variation proportional to the Pr doping level, all the samples show similar spectra as the Pr_2O_3 reference sample (red curve), which indicates that Pr ions in the films possess dominantly the +3 valence state. In the spectra, two prominent spin–orbit doublets denoted by a/a_1 and b/b_1 are observed, which are induced respectively by core holes and valence band holes. These peaks refer to Pr $3d_{3/2}$ (a/b) and Pr $3d_{5/2}$ (a_1/b_1) final states, as marked in the figure. An additional weak peak labeled by t_1 (black dash lines) appears at ~958 eV, which is related to the multiplet effect.[55] It is well-known that Pr oxides form mixed valence oxides and Pr^{4+} normally coexists with Pr^{3+}. The doublet c/c_1 (946 eV/967 eV, marked by gray dash lines) is suggested to be a signature for the Pr^{4+} presence. Nevertheless, according to a meticulous XPS study[56] on PrO_2 and Pr_2O_3, even Pr 3d spectra of complete Pr^{3+} also show broad c/c_1 peaks, which is rather similar to what we observed from the reference spectrum. Therefore, different from Ce 3d spectra, no reliable approach exists to quantitatively analyze Pr^{3+} concentration in the film. Even a qualitative judgment of Pr^{4+} presence in a Pr-oxide film is not straightforward by laboratory-based XPS.[57]

The O 1s spectra of the films are also probed, as shown in Figure 2c. O 1s spectrum of pure CeO_2 film shows a single peak located at ~530 eV (gray peak), which corresponds to the O–Ce bonds. With Pr doping into the film, the main peak does not shift and an additional peak located at ~532.2 eV (blue peak) appears, the relative intensity of which increases along with Pr concentration. The O peak at a higher binding energy (O_{HBE}) is associated with the oxygen in form of OH group due to the hygroscopic nature of Pr_2O_3.[58] Pr_2O_3 tends to absorb atmospheric water, thus yielding the O_{HBE} peak in the mixed

oxide films and the O_{HBE} ratio increases with Pr_2O_3 concentration in the films.[59,60]

As the Ce valence state is an important issue for subsequent FM discussion, it is necessary to investigate if Ce^{3+} exists in the volume of the film, considering that XPS is only a surface sensitive technique and the slight amount of Ce^{3+} existing in doped and pure CeO_2 films is due to the surface reduction effects under UHV ambiance in the XPS chamber. We therefore perform X-ray absorption near edge structure spectroscopy (XANES) measurements and the spectra of Ce L_{III} edge are shown in Figure 3. A spectrum (green curve, realized in transmission mode) of crystalline CeO_2 powder, which is considered to be stoichiometric and thus contains no detectable Ce^{3+} ions, is given as a reference. Apparently, all the films present curves similar to the reference powder one. This observation indicates that Ce shows only a +4 valence state in oxide films and Pr^{3+} doping does not yield a detectable level of trivalent Ce, which corroborates the XPS measurements. In Figure 3, the spectra show two main peaks, A and B, both of which correspond to Ce^{4+} final states. This multiple final states feature originates from the hybridization between O 2p and Ce 4f (5d) states.[61] Peak A is associated with a core excited Ce^{4+} final state of $2p4f^05d^1$ whereas peak B corresponds to a Ce^{4+} $2p4f^15d^1v$ final state related to covalence between Ce 4f and O 2p, in which v represents a hole left by the excited electron from the valence band (O 2p shell) to the Ce 4f shell.[62,63] A prior XANES study on CeO_2 nanoparticles pointed out that the spectral component B would shift to a lower energy by ~3 eV and its intensity would increase, when Ce^{3+} is present in the material.[64] None of these variations are observed in our mixed films. The XPS combined with XANES results suggest that, although CeO_2 in nanoparticles form could yield a reduction in the valence of the Ce^{4+} ions to Ce^{3+}, doping with other trivalent (or divalent) elements is probably the only effective way to induce major $Vo^{\cdot\cdot}$ concentrations in CeO_2 films, owing to the difficulty of Ce^{3+} formation in them. In other words, $Vo^{\cdot\cdot}$ are introduced by the substitution of Ce^{4+} by Pr^{3+} in our systems but all remaining Ce ions remain in the +4 valence state.

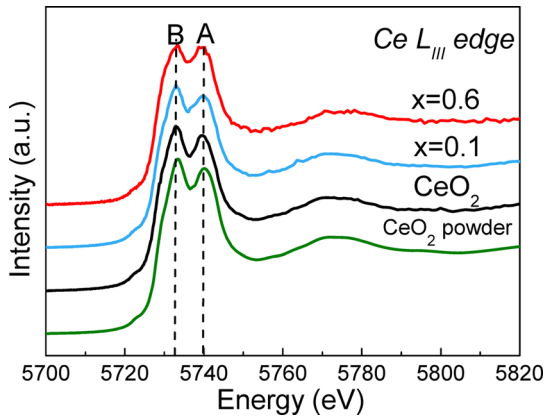

Figure 3. XANES spectra at Ce L_{III} edge for CeO_2, $Ce_{0.9}Pr_{0.1}O_{2-\delta}$ and $Ce_{0.4}Pr_{0.6}O_{2-\delta}$ films as well as a reference obtained from CeO_2 powder. Two principal peaks are denoted as A and B.

3.3. Oxygen Vacancy and Other Defects Detection. When another element is doped into the CeO_2 lattice, defects form due to different ion radii and valence states. To possibly clarify the correlation between defects and functional properties (e.g., RTFM) in the films, it is necessary to understand more details of defects at a local level. Raman spectroscopy is a powerful tool for this purpose thanks to its strong sensitivity to the phonon characterization, reflecting deviations from the ideal crystalline nature of the materials. Raman spectra performed on our $Ce_{1-x}Pr_xO_{2-\delta}$ films are shown in Figure 4a,

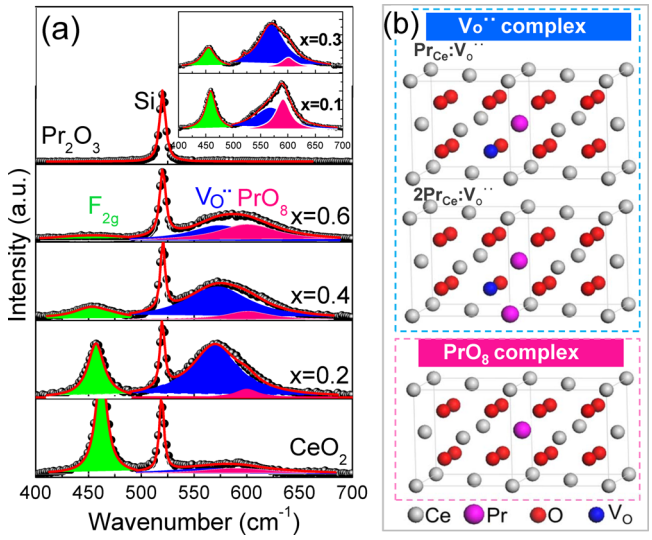

Figure 4. (a) UV Raman spectra of $Ce_{1-x}Pr_xO_{2-\delta}$/Si(111) samples (x = 0−1) with fitted curves. Spectra of thicker films are shown in inset. (b) Defect crystal structures of $Vo^{\cdot\cdot}$ and PrO_8 complexes.

with fitting curves represented by Lorentzian components. A UV laser with λ = 325 nm was selected as the excitation source because, compared to visible lasers that have lower energy and only provide strong signals from the substrate,[65] it has higher energy thus allowing resonance Raman and permits for strong enough cross section to obtain detectable signals from nanometric-scaled thin films.

In Figure 4a, the most intense Raman peak for all samples (~24 nm) appears at ~520 cm^{-1}, which corresponds to the transverse optical mode of the Si substrate.[66] Interestingly, this Si-related signal strongly decreases but is still visible for the ~87 nm films spectra shown in the inset of Figure 4a, which indicates that the detected spectra are still from the whole volume of oxide films. Apart from the Si Raman mode, three additional peaks arise from the oxide films. The Raman peak located at ~460 cm^{-1} (filled by green) refers to the triply degenerate F_{2g} Raman-active mode of CeO_2 crystallizing in a fluorite lattice (space group O_h^5). It is known that the Raman active modes of the fluorite lattice are represented by $A_{1g} + E_g + F_{2g}$.[67] Under our Raman spectroscopy conditions with an unpolarized laser and backscattering configuration, only the F_{2g} mode can be detected, which can be viewed as a symmetric breathing mode of the O atoms around each cation.[34] For the Pr-doped CeO_2 films, there are two other Raman modes positioned at ~570 cm^{-1} (filled by blue) and ~600 cm^{-1} (filled by pink), respectively, both of which originate from defect structures in the lattice. According to theoretical calculations carried out by Nakajima et al.[68] on Raman spectra of doped CeO_2 crystals, the blue peak located at ~570 cm^{-1} is assigned to defect spaces including an oxygen vacancy, thus breaking the O_h symmetry of the fluorite lattice. The pink peak located at ~600 cm^{-1} is assigned to a MO_8-type complex without having any $Vo^{\cdot\cdot}$ (in this case, only PrO_8-type, considering the absence of Ce^{3+} in our films), where a dopant cation is surrounded by

eight nearest-neighbor O^{2-} ions thus the O_h symmetry is maintained. A fairly weak defect-related peak appears as well in pure CeO_2 spectrum. This can be attributed to the Ce^{4+}–Pr^{3+}exchanging at the interface[69] (thus defects related modes) due to the ~2 nm Pr_2O_3 buffer layer that is deposited prior to the CeO_2 film to ensure the high crystalline quality of CeO_2 films (i.e., to suppress the interface reaction). Atomic configuration details of the defects are illustrated in Figure 4b. It is also illustrated that there are two possibilities for the $Vo^{\cdot\cdot}$-related complex at 570 cm^{-1}, namely, Pr_{Ce}:$Vo^{\cdot\cdot}$ with one dopant around $Vo^{\cdot\cdot}$ or $2Pr_{Ce}$:$Vo^{\cdot\cdot}$ with two dopants around $Vo^{\cdot\cdot}$. Furthermore, a detailed Raman study on $Ce_{0.8}M_{0.2}O_{2-\delta}$ (M = Zr, La, Pr, Lu, Y, Gd, Sm) nanoparticles[70] shows that although other dopants yield both $Vo^{\cdot\cdot}$ and MO_8 peaks, Zr^{4+}- and Pr^{3+}-doped CeO_2 samples demonstrate almost only MO_8 and $Vo^{\cdot\cdot}$ peaks, respectively. Therefore, the MO_8-type complex can be mainly attributed to the ion radii differences between Ce and the dopant (Zr^{4+} has the same valence state as Ce^{4+}) and Pr^{3+} can induce more $Vo^{\cdot\cdot}$ compared to other RE dopants for the same dopant concentration.

Increasing the Pr concentration gradually alters the lattice structure and thus the defect population. Globally, the intensities of all the Raman peaks of oxides are reduced with the increase of the Pr content (x) and particularly, only the Si peak can be observed in the spectrum of the pure Pr_2O_3 reference sample. This is related to two effects: (i) a structure transition from fluorite to bixbyite as x increases. Pr^{3+} doping gradually destroys the fluorite (CeO_2) symmetry and eventually leads to a bixbyite structure (Pr_2O_3); (ii) the fluorescence effect from Pr_2O_3 that reduces the detectable Raman signal of oxide films and this effect becomes stronger as x increases. Because the band gap of Pr_2O_3 is 3.9 eV, which is higher than 2.4 eV of CeO_2, more Pr doping probably leads to a stronger fluorescence effect. Similar behavior has been reported for Pr- or Tb-doped CeO_2 nanoparticles.[34,71] Figure 5a displays the variation of the F_{2g} mode as the Pr concentration increases, in which the peak position (black plotting) progressively shifts to a lower energy (from 460.1 cm^{-1} for x = 0 to 453.0 cm^{-1} for x = 0.6) and the full width at half-maximum (fwhm, blue plotting) undergoes a continuous enlargement (from 13.5 for x = 0 to 84.6 for x = 0.6). Several factors can contribute to the changes of F_{2g} peak including phonon confinement, strain, defects, etc.[72,73] In this case, the systematic peak shift mainly correlates to the lattice expansion, considering that lattice constant of Pr_2O_3 ($(1/2) \cdot a_{Pr_2O_3}$ = 5.576 Å) is larger than that of CeO_2 (a_{CeO_2} = 5.411 Å) whereas the peak broadening is related to Pr-doping induced defects, which also contribute to the progressive reduction of F_{2g} Raman mode intensity (local symmetry break of CeO_2 lattices). This result also reveals that Pr dopants have incorporated into CeO_2 lattice and forms solid solutions with ceria, which is in good agreement with XRD measurements.

Figure 5b,c shows the changing of defect-related peaks as a function of increasing Pr concentration. Figure 5b demonstrates that the $Vo^{\cdot\cdot}$ peak shifts to higher energy, particularly in the range of x = 0.2–0.4, which is related to the increase of the $2Pr_{Ce}$:$Vo^{\cdot\cdot}$-complex concentration (compared to Pr_{Ce}:$Vo^{\cdot\cdot}$ complexes).[68] In principle, due to statistics and energy considerations (strained local environments of Pr^{3+} traps $Vo^{\cdot\cdot}$), this change in defect microstructure is to be expected.[74] We note here that this observation is important for subsequent FM discussion based on the proposed F-center mechanism.

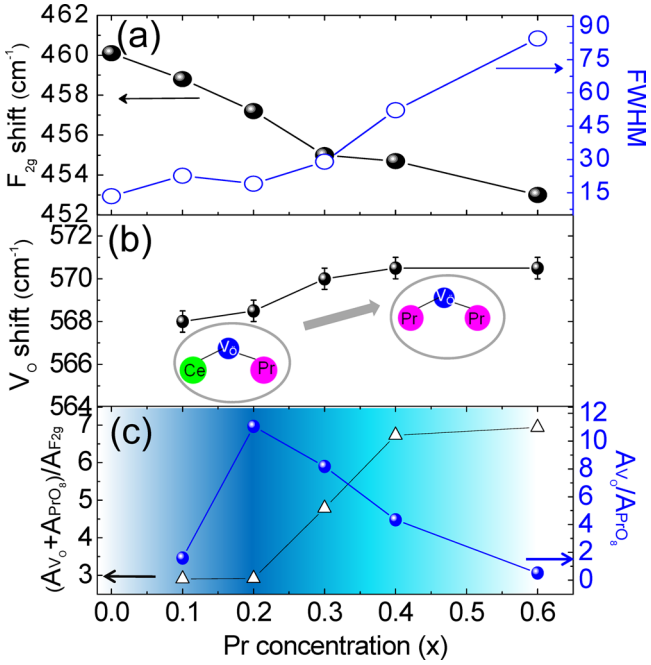

Figure 5. Raman modes variation as a function of Pr concentration (a) F_{2g} peak shift and width changing; (b) $Vo^{\cdot\cdot}$ peak shift suggesting a transition from Pr_{Ce}:$Vo^{\cdot\cdot}$ to 2 Pr_{Ce}:$Vo^{\cdot\cdot}$; (c) area ratio of defects/F_{2g} and $Vo^{\cdot\cdot}/PrO_8$.

The ratio of defect areas compared to F_{2g} peak area, $(A_{Vo^{\cdot\cdot}} + A_{PrO_8})/A_{F_{2g}}$ as a function of Pr content is plotted in Figure 5c by the black curve, which suggests that more Pr doping introduces more defects into the CeO_2 lattice. This result points again to a CeO_2 crystal structure with heavily distorted local structure due to intensive Pr-doping. The blue curve in Figure 5c plots the variation of relative $Vo^{\cdot\cdot}$ ratio, i.e., $A_{Vo^{\cdot\cdot}}/A_{PrO_8}$. When the Pr concentration increases, it first experiences a robust increase from x = 0.1 to x = 0.2 and reaches a maximum at x = 0.2. After that, it progressively decreases and drops to a quite small value for the film with x = 0.6. Therefore, x = 0.2 Pr-doping turns out to be the most effective doping level to create $Vo^{\cdot\cdot}$ defects in CeO_2 lattices. Further increase of the Pr concentration only results in higher PrO_8-complex concentration. Moreover, larger Pr-doping concentration could also lead to phase transition from fluorite to bixbyite and degrade thus the crystalline quality of the mixed films.

To clarify this point, high-resolution transmission electron microscopy (HRTEM) measurements were performed on the x = 0.2 and x = 0.6 samples. Figure 6a shows a TEM cross-sectional image of the $Ce_{0.8}Pr_{0.2}O_{2-\delta}$/Si(111) heterostructure. The oxide film demonstrates a high crystalline quality with homogeneous color contrast. An amorphous layer can also be seen at the interface corresponding to SiO_2 or silicate formed during the growth by interface oxidation (for more interface details, see Figure S3, Supporting Information). Figure 6b displays a fast Fourier transformation (FFT) image on the oxide film region, which is a typical diffraction pattern of fluorite lattice along the ⟨111⟩ direction (marked by yellow circles and spots; details are also given).[42] A similar analysis was carried out on the Pr-rich $Ce_{0.4}Pr_{0.6}O_{2-\delta}$/Si(111) sample, which shows inhomogeneous color contrast in the TEM image (Figure 6c), thus lower crystalline quality and, in the FFT pattern (Figure 6d), an extra series of diffraction spots (marked

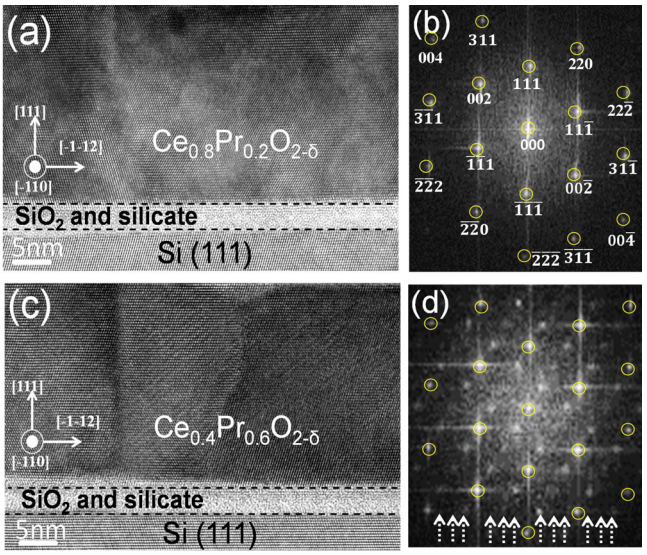

Figure 6. Cross-sectional TEM images of $Ce_{0.8}Pr_{0.2}O_{2-\delta}$/Si(111) (a) and $Ce_{0.4}Pr_{0.6}O_{2-\delta}$/Si(111) (c) heterostructures and corresponding FFT patterns (b) and (d).

by dotted arrows) also appears, which indicates the presence of a bixbyite lattice structure of the oxide film. The coexistence of fluorite lattice and bixbyite lattice, as well as larger lattice mismatch between Pr_2O_3 and Si compared to CeO_2/Si system, is thus responsible for the degradation of the film quality and the change in defect population.

3.4. FM Properties of $Vo^{\cdot\cdot}$-Engineered Pr-Doped CeO_2 Thin Films. The FM properties of $Ce_{1-x}Pr_xO_{2-\delta}$/Si(111) (x = 0.1, 0.2, 0.3, and 0.4) samples were investigated at RT by SQUID. The samples were cut by a diamond scribe and always handled using Teflon tweezers to avoid any iron contact contamination, which would induce unwanted magnetization.[75] Figure 7a shows the raw experimental data, in which x = 0.1 (blue) and x = 0.2 (orange) samples exhibit RTFM behavior while the x = 0.3 (olive) and x = 0.4 (violet) samples seems to be diamagnetic. A blank Si substrate was also measured (dashed line in black) as a reference and it shows a diamagnetic feature. The curves after subtracting the diamagnetic contribution from the Si substrate are shown in Figure 7b. It can be observed that the least Pr-doped CeO_2 sample with x = 0.1 shows a clear RTFM behavior with an open $M-H$ hysteretic loop (Figure 7b: zoomed inset). The coercivity (H_c) and saturation magnetization (M_s) of this sample are ~20 Oe and 0.45 emu/g, respectively. It is noted here that values of coercivity can be impacted by the remnant field of superconducting magnets in magnetometers. In our case, from measurements of the nonmagnetic Pr-doped CeO_2 films, we estimate magnetic field errors during SQUID measurements due to residual currents in the magnet and/or flux pinning to be only ~10 Oe. The FM is strongly enhanced when the Pr-concentration is increased to x = 0.2. As shown in Figure 7b, the x = 0.2 sample displays a well-defined hysteretic loop as well as a much larger RTFM with the H_c and M_s being ~55 Oe and ~1.80 emu/g, respectively. This is a notable result because the M_s value is 2 orders of magnitude higher than the RTFM values found in

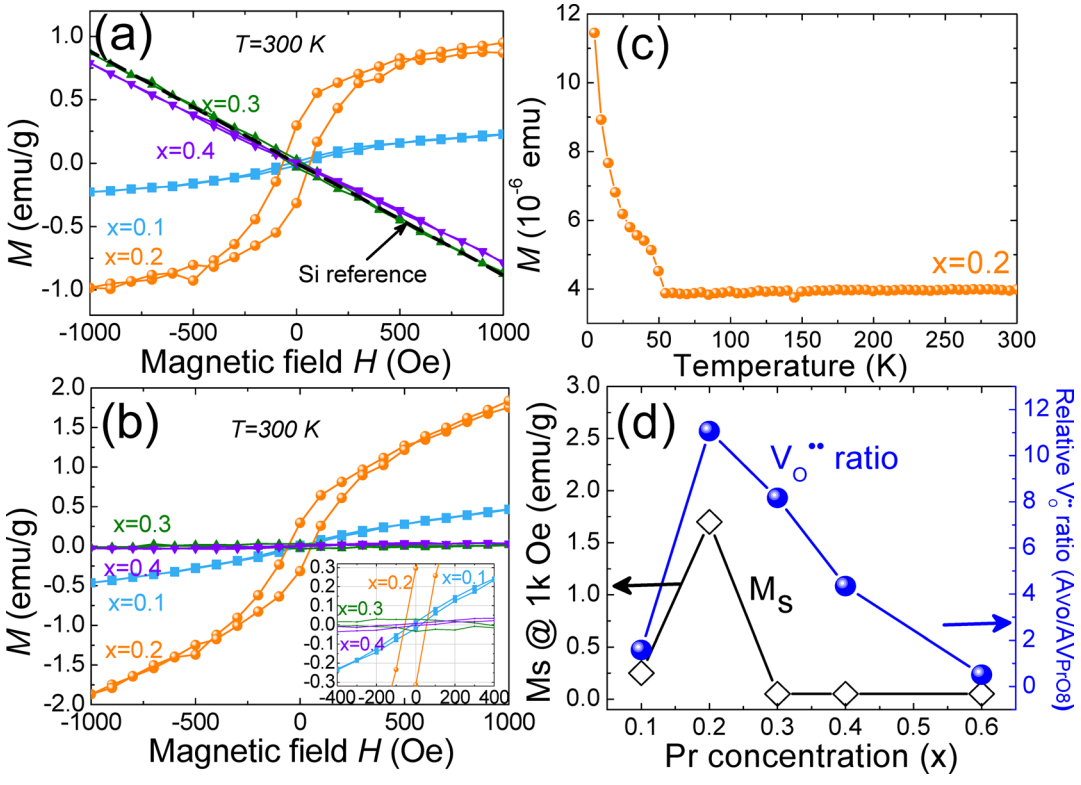

Figure 7. Room temperature $M-H$ curves of the samples with x = 0.1–0.4: (a) raw experimental data in which the Si reference signal is shown by a black dashed line; (b) data after subtracting the diamagnetic component of the Si substrate. Insets show the details of magnetic hysteresis loops. (c) Temperature dependent field-cooling magnetic moment curve of x = 0.2 sample taken under a magnetic field of 600 Oe. (d) Variation of M_s (extracted from (b), black curve) as a function of Pr concentration, compared with the variation of relative $Vo^{\cdot\cdot}$ ratio (blue curve) extracted from Raman analysis in Figure 5c (area ratio of $Vo^{\cdot\cdot}/PrO_8$).

dx.doi.org/10.1021/am502238w | ACS Appl. Mater. Interfaces 2014, 6, 17496–17505

undoped/doped CeO_2 nanoparticles (M_s is generally in the 10^{-2} emu/g range.[16,17,32,33,36,76−78]). Concerning CeO_2-based thin film systems, our results are comparable with the RTFM with a giant magnetic moment reported by Tiwari et al. in Co-doped CeO_2 epitaxial films on $LaAlO_3$(001) substrates.[28] The temperature dependent field-cooling magnetic moment curve of the $Ce_{0.8}Pr_{0.2}O_{2-\delta}$/Si sample ($x$ = 0.2) was collected under a magnetic field of 600 Oe, as shown in Figure 7c. The magnetic moment shows a rather slight modification above 50 K by increasing the temperature, therefore indicating a Curie temperature well above 300 K. The increase of the magnetic moment below 55 K is probably related to paramagnetic contributions, namely, the alignment of isolated magnetic moments along with the applied magnetic field.[15] The x = 0.3 and 0.4 samples show that further increasing the Pr concentration beyond x = 0.2 dramatically degrades the FM behavior of the samples: the SQUID signals are strongly disturbed by the diamagnetic Si substrate, as shown by Figure 7b and the corresponding inset.

Consider now the origin of the different magnetic properties of samples with different Pr-doping concentrations. It is known that stoichiometric CeO_2 is diamagnetic with Ce^{4+} ions in the $4f^0$ electron configuration, which has no unpaired electron and thus no net magnetic moment. Ce^{3+} ions ($4f^1$) are paramagnetic due to the one unpaired electron in a 4f orbital. It is worth noting here that the XPS and XANES results point to the absence of Ce^{3+} in $Ce_{1-x}Pr_xO_{2-\delta}$ films. Meanwhile, Pr^{4+} ($4f^1$, being isoelectronic with Ce^{3+}) and Pr^{3+} ions ($4f^2$, with two unpaired electrons) both have net magnetic moments and Pr-oxides are paramagnetic.[79]

Up to now, there is an incomplete understanding on the origin of RTFM in doped CeO_2 as well as in other diluted magnetic oxides. Although a lot of observations of RTFM in these systems have been reported, some doubts were also raised arguing that the RTFM could possibly stem from contaminations during sample handling or from the formation of secondary metal phases or metal clusters in oxides. However, an increasing number of experimental and theoretical results[19−33] show that the RTFM is an intrinsic property of such materials and strongly correlates to the defects in the oxides. In particular, in a quite recent study, Prestgard et al. reported[29] a comparison of different magnetic properties in CeO_2-based systems originated from homogeneous doping, a mixture of doping and metal cluster formation, and purely from metal clustering. It was concluded that RTFM property is intrinsic in homogeneously doped CeO_2 system and is related to the defects.[28,29] For our $Ce_{1-x}Pr_xO_{2-\delta}$ films, we note here that all the samples were cut by a diamond scribe and were always handled using Teflon tweezers to avoid any metal contamination. Furthermore, $Ce_{1-x}Pr_xO_{2-\delta}$ films form solid solutions[17,34,35] and neither second metallic phases nor metal clusters can be observed from our XRD, Raman and HRTEM results. Therefore, the observed RTFM in our Pr-doped CeO_2 films is the intrinsic property and is related to the defects, particularly to the oxygen vacancies ($Vo^{\cdot\cdot}$) in the oxides. We plot the variation of the M_s of different $Ce_{1-x}Pr_xO_{2-\delta}$ films (cf. Figure 7b) as a function of Pr concentration x in Figure 7d (black curve) and it is compared with the variation of relative $Vo^{\cdot\cdot}$ ratio extracted by Raman analysis (blue curve, cf. Figure 5c). Interestingly, they show a similar tendency, indicating the RTFM in $Ce_{1-x}Pr_xO_{2-\delta}$ films is indeed related to $Vo^{\cdot\cdot}$ in the oxides. The relationship between RTFM and $Vo^{\cdot\cdot}$ can be clarified in more detail by using the F-center exchange mechanism (FCE) model. FCE has been successfully used to explain the RTFM in many oxides in the form of nanoparticles such as ZnO, TiO_2, SnO_2, CeO_2, Al_2O_3, etc.[25] When an $Vo^{\cdot\cdot}$ is formed, two electrons are left behind that can be trapped in $Vo^{\cdot\cdot}$. The FCE mechanism categorizes $Vo^{\cdot\cdot}$ (color center, i.e., F-center) into three groups: (1) the F^{2+} center with no trapped electrons; (2) the F^+ center with one trapped electron that can mediate FM interaction; (3) F^0 center with two trapped electrons that can only mediate weak antiferromagnetic (AFM) interactions. For the F^+ center, the locally trapped electron is confined in a hydrogenic orbital (radius $r_H = \varepsilon(m/m^*)a_0$, where ε is the dielectric constant, m is the electron mass, m^* is the effective electron mass of the donor electrons, and a_0 is the Bohr radius of 53 pm) around $Vo^{\cdot\cdot}$ and can possibly form bound magnetic polarons (BMP) by ordering the dopant electron spin neighboring the oxygen vacancies. As the $Vo^{\cdot\cdot}$ density increases, the hydrogenic orbitals associated with randomly positioned $Vo^{\cdot\cdot}$ overlap and when the $Vo^{\cdot\cdot}$ density exceeds a percolation threshold, long-range FM can be established in the oxide.[25]

In undoped oxygen deficient CeO_2 nanoparticles, two main $Vo^{\cdot\cdot}$-related complexes can exist: Ce^{4+}−$Vo^{\cdot\cdot}$−Ce^{3+} and Ce^{3+}−$Vo^{\cdot\cdot}$−Ce^{3+}. The former one forms an F^+ center because the two electrons left by $Vo^{\cdot\cdot}$ are trapped respectively on a Ce^{4+} ion and on the $Vo^{\cdot\cdot}$ hydrogenic orbital. The Ce^{3+}−$Vo^{\cdot\cdot}$−Ce^{3+}complex, however, forms a F^{2+} center because both electrons are trapped on Ce^{4+} ions. When Pr is doped into CeO_2, Paunović et al.[36] recently reported that the Pr-doping suppresses the inherent RTFM of CeO_2 nanocrystals induced by the Ce^{4+}−$Vo^{\cdot\cdot}$−Ce^{3+} (F^+ center) complex. Such suppression of RTFM by Pr-doping has been attributed to the formation of complexes like Pr^{3+}−$Vo^{\cdot\cdot}$−Ce^{3+} and Pr^{3+}−$Vo^{\cdot\cdot}$−Pr^{3+} (F^{2+} centers) that do not mediate FM ordering. On the basis of this work,[36] we clarify different F centers in our $Ce_{1-x}Pr_xO_{2-\delta}$ epitaxial films. Different from its nanocrystal counterpart,[36] our Pr-doped CeO_2 thin films do not contain Ce^{3+} ions; hence, two $Vo^{\cdot\cdot}$-related complexes, Ce^{4+}−$Vo^{\cdot\cdot}$−Pr^{3+} and Pr^{3+}−$Vo^{\cdot\cdot}$−Pr^{3+}, yield an F^+ center and F^{2+} center, respectively, as shown in Figure 8. The r_H in this case can be estimated as 46 Å, using m^*/m = 0.3 for CeO_2 with a fluorite structure.[76]

When the Pr^{3+} concentration is quite low, the magnetic moments are far apart and cannot be coupled by F^+ centers. As the Pr content x increases, according to our detailed Raman study (Figure 5c), the relative $Vo^{\cdot\cdot}$ concentration also increases when x < 0.2 and, in this range, the Ce^{4+}−$Vo^{\cdot\cdot}$−Pr^{3+} complex (F^+ center) is dominant (Figure 5b). Provided that F^+ center

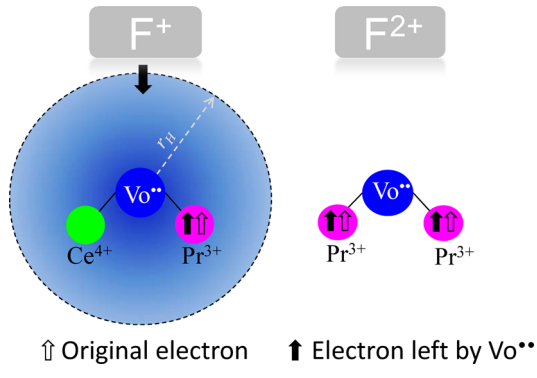

Figure 8. Illustration of F^+ and F^{2+} centers in the films, which mediate and do not mediate FM ordering, respectively.

density exceeds the magnetic percolation threshold value $n_{Vo^{\cdot\cdot}}$, the F^+ centers overlap, leading to the spin polarization of the majority of Pr ions. The critical value $n_{Vo^{\cdot\cdot}}$ can be estimated by $\gamma^3(n_{Vo^{\cdot\cdot}}/n_0) \approx 4.3$, where $\gamma = \varepsilon(m/m^*)$ and $n_0 = 5 \times 10^{28}$ m^{-3} is the oxygen density in CeO_2,[25] thus $n_{Vo^{\cdot\cdot}} \approx 3 \times 10^{23}$ m^{-3}. We postulate that our $x = 0.1$ sample already reaches this condition, thus showing the RTFM behavior (Figure 7b). In the $x = 0.2$ sample, F^+ center density is augmented, hence it shows strongly enhanced RTFM properties with higher saturation magnetization. The effective magnetic moment μ_{eff} per Pr ion can be calculated using the equation: $\mu_{eff} = M_s/N$, where M_s is the saturation magnetization and N is the number of Pr atoms per cubic meter. Considering that the number of Ce atoms in nondoped CeO_2 oxides is 2.5×10^{28} m^{-3}, the N_{Pr} values in $x = 0.1$ and $x = 0.2$ samples are 2.5×10^{27} m^{-3} and 5×10^{27} m^{-3}, respectively. Therefore, the μ_{eff} values per Pr ion in the $x = 0.1$ and $x = 0.2$ samples are 0.07 μ_B and 0.15 μ_B, respectively ($\mu_B = 9.27 \times 10^{-24}$ $A{\cdot}m^2$).

Furthermore, compared to the RTFM found in CeO_2 nanoparticles, the M_s value of the $x = 0.2$ sample is rather giant. We attribute this to the higher capability of creating $Vo^{\cdot\cdot}$ (thus F^+ center) in CeO_2 by Pr^{3+}-doping instead of forming Ce^{3+} ions by oxygen depletion in the CeO_2 surface areas of the nanoparticles. A Raman study on the undoped CeO_2 nanoparticles[80] demonstrates that Ce^{3+} ions are preferably located in MO_8-type (here M = Ce^{3+}) complexes rather than $Vo^{\cdot\cdot}$ complexes. However, further increasing the Pr concentration ($x > 0.2$) in doped CeO_2 films could create F^{2+} and F^0 centers, thus dramatically decreasing the F^+ center density in several ways: (i) more Pr^{3+}–$Vo^{\cdot\cdot}$–Pr^{3+}complexes form and become dominant (Figure 5b), (ii) PrO_8-type complex defects increase (Figure 5c), and (iii) gradual structure phase transition from fluorite lattices to more distorted bixbyite lattices (Figure 6). F^{2+} and F^0 centers cannot mediate the FM interaction, and their formation causes the decreasing of F^+ center density below the percolation threshold; consequently, samples with $x > 0.2$ show a sudden disappearance of RTFM properties. In addition, another effect that could possibly suppress FM ordering in the case of higher Pr concentrations is the superexchange interaction between nearest-neighbor Pr ions via oxygen anions, which is antiferromagnetic, thus hindering the establishment of long-range FM order.

4. Conclusions. In conclusion, we demonstrate the growth of Pr-doped ceria epitaxial thin films showing RTFM on silicon substrates. Pr^{3+} dopants are incorporated into ceria lattices, thus forming solid solutions and do not affect the +4 valence state of Ce ions in ambient conditions. Raman spectroscopy turns out to be a powerful tool to explore the microscopic mechanism of defects formation in the $Ce_{1-x}Pr_xO_{2-\delta}$ films. Pr doping effectively creates oxygen vacancies ($Vo^{\cdot\cdot}$) in CeO_2 lattices, despite the introduction at the same time of other defects like PrO_8-type complexes. Elevated Pr-concentration causes fluorite-to-bixbyite phase transition and degrades the crystalline quality of the films. The FM properties of the films strongly correlate to the relative $Vo^{\cdot\cdot}$ concentration (in particular, $Vo^{\cdot\cdot}$ with one nearest-neighbor Pr^{3+}) and this behavior can be well explained by the F-center exchange mechanism. These films initially show enhanced RTFM as the $Vo^{\cdot\cdot}$ amount increases but experience sudden disappearance of RTFM due to the increasing importance of alternative defect formation mechanism which probably leads to the decreasing of F^+ center density below the percolation threshold value. The $Ce_{0.8}Pr_{0.2}O_{2-\delta}$ film turns out to contain the highest F^+ center density, thus showing RTFM with a saturation magnetization $M_s \sim 1.8$ emu/g. These results can not only facilitate the understanding of the origin of RTFM in diluted magnetic oxides but also highlight the possibility to develop future monolithic magnetic-optic or spintronic devices using crystalline oxide thin film systems on Si substrates.

■ ASSOCIATED CONTENT

Supporting Information

(1) Optimization of the growth conditions of $Ce_{1-x}Pr_xO_{2-\delta}$ films, including growth temperature, oxygen partial pressure, and the growth of buffer layers, (2) 7 × 7 reconstruction of Si (111) substrate prior to the oxide growth, and (3) specular θ-2θ XRD measurements on $Ce_{1-x}Pr_xO_{2-\delta}$ films over a wide 2θ range (20°–100°). This material is available free of charge via the Internet at http://pubs.acs.org.

■ AUTHOR INFORMATION

Corresponding Author

*G. Niu. E-mail: gang@ihp-microelectronics.com.

Notes

The authors declare no competing financial interest.

■ ACKNOWLEDGMENTS

Dr. Gang Niu gratefully acknowledges funding support by Alexander von Humboldt foundation in form of an AvH Post-Doc fellowship. This work is partly supported by "Deutsche Forschungsgemeinschaft" (DFG).

■ REFERENCES

(1) Norton, D. P. Synthesis and Properties of Epitaxial Electronic Oxide Thin-Film Materials. *Mater. Sci. Eng.* **2004**, *R 43*, 139–247.

(2) Reiner, J. W.; Kolpak, A. M.; Segal, Y.; Garrity, K. F.; Ismail-Beigi, S.; Ahn, C. H.; Walker, F. J. Crystalline Oxides on Silicon. *Adv. Mater.* **2010**, *22*, 2919–2938.

(3) Chanthbouala, A.; Garcia, V.; Cherifi, R. O.; Bouzehouane, K.; Fusil, S.; Moya, X.; Xavier, S.; Yamada, H.; Deranlot, C.; Mathur, N. D.; Bibes, M.; Barthélémy, A.; Grollier, J. A Ferroelectric Memristor. *Nat. Mater.* **2012**, *11*, 860–864.

(4) Niu, G.; Yin, S.; Saint-Girons, G.; Gautier, B.; Lecoeur, P.; Pillard, V.; Hollinger, G.; Vilquin, B. Epitaxy of $BaTiO_3$ Thin Film on Si(001) Using a $SrTiO_3$ Buffer Layer for Non-volatile Memory Application. *Microelectron. Eng.* **2011**, *88*, 1232–1235.

(5) Baek, S. H.; Park, J.; Kim, D. M.; Aksyuk, V. A.; Das, R. R.; Bu, S. D.; Felker, D. A.; Lettieri, J.; Vaithyanathan, V.; Bharadwaja, S. S. N.; Bassiri-Gharb, N.; Chen, Y. B.; Sun, H. P.; Folkman, C. M.; Jang, H. W.; Kreft, D. J.; Streiffer, S. K.; Ramesh, R.; Pan, X. Q.; Trolier-McKinstry, S.; Schlom, D. G.; Rzchowski, M. S.; Blick, R. H.; Eom, C. B. Giant Piezoelectricity on Si for Hyperactive MEMS. *Science* **2011**, *334*, 958–961.

(6) Abel, S.; Stöferle, T.; Marchiori, C.; Rossel, C.; Rossell, M. D.; Erni, R.; Caimi, D.; Sousa, M.; Chelnokov, A.; Offrein, B. J.; Fompeyrine, J. A Strong Electro-optically Active Lead-Free Ferroelectric Integrated on Silicon. *Nat. Commun.* **2012**, *4*, 1671-1–1671-6.

(7) Sando, D.; Agbelele, A.; Rahmedov, D.; Liu, J.; Rovillain, P.; Toulouse, C.; Infante, I. C.; Pyatakov, A. P.; Fusil, S.; Jacquet, E.; Carrétéro, C.; Deranlot, C.; Lisenkov, S.; Wang, D.; Breton, J.-M. L.; Cazayous, M.; Sacuto, A.; Juraszek, J.; Zvezdin, A. K.; Bellaiche, L.; Dkhil, B.; Barthélémy, A.; Bibes, M. Crafting the Magnonic and Spintronic Response of $BiFeO_3$ Films by Epitaxial Strain. *Nat. Mater.* **2013**, *12*, 641–646.

(8) Chen, C.-H.; Chang, I. Y.-K.; Lee, J. Y.-M.; Chiu, F.-C. Electrical Characterization of CeO_2/Si Interface Properties of Metal-Oxide Semiconductor Field-Effect Transistors with CeO_2 Gate Dielectric. *Appl. Phys. Lett.* **2008**, *92*, 043507-1–043507-3.

(9) Boikov, Y. A.; Claeson, T.; Erts, D. CeO_2 Compatibility with $YBa_2Cu_3O_7$ in Superconducting-Film Multilayers. *Phys. Rev. B* **1997**, *56*, 11312−11319.
(10) He, Y.; Yang, B.; Cheng, G. On the Oxidative Coupling of Methane with Carbon Dioxide over CeO_2/ZnO Nanocatalysts. *Catal. Today* **2004**, *98*, 595−600.
(11) Mogensen, M.; Primdahl, S.; Jorgensen, M. J.; Bagger, C. Composite Electrodes in Solid Oxide Fuel Cells and Similar Solid State Devices. *J. Electroceram.* **2000**, *5*, 141−152.
(12) Izu, N.; Shin, W.; Murayama, N.; Kanzaki, S. Resistive Oxygen Gas Sensors Based on CeO_2 Fine Powder Prepared Using Mist Pyrolysis. *Sens. Actuators, B* **2002**, *87*, 95−98.
(13) Ackland, K.; Monzon, L. M. A.; Venkatesan, M.; Coey, J. M. D. Magnetism of Nanostructured CeO_2. *IEEE Trans. Magn.* **2011**, *47*, 3509−3512.
(14) Han, X.; Lee, J.; Yoo, H.-I. Oxygen-Vacancy-Induced Ferromagnetism in CeO_2 from First Principles. *Phys. Rev. B* **2009**, *79*, 100403-1−100403-4.
(15) Fernandes, V.; Mossanek, R. J. O.; Schio, P.; Klein, J. J.; de Oliveira, A. J. A.; Ortiz, W. A.; Mattoso, N.; Varalda, J.; Schreiner, W. H.; Abbate, M.; Mosca, D. H. Dilute-Defect Magnetism: Origin of Magnetism in Nanocrystalline CeO_2. *Phys. Rev. B* **2009**, *80*, 035202-1−035202-7.
(16) Singhal, R. K.; Kumari, P.; Samariya, A.; Kumar, S.; Sharma, S. C.; Xing, Y. T.; Saitovitch, E. B. Role of Electronic Structure and Oxygen Defects in Driving Ferromagnetism in Nondoped Bulk CeO_2. *Appl. Phys. Lett.* **2010**, *97*, 172503-1−172503-3.
(17) Dimri, M. C.; Khanduri, H.; Kooskora, H.; Subbi, J.; Heinmaa, I.; Mere, A.; Krustok, J.; Stern, R. Ferromagnetism in Rare Earth Doped Cerium Oxide Bulk Samples. *Phys. Status Solidi A* **2012**, *209*, 353−358.
(18) Wen, Q.-Y.; Zhang, H.-W.; Song, Y.-Q.; Yang, Q.-H.; Zhu, H.; Xiao, J. Q. Room-Temperature Ferromagnetism in Pure and Co Doped CeO_2 Powders. *J. Phys.: Condens. Matter* **2007**, *19*, 246205-1−246205-7.
(19) Sharma, P.; Gupta, A.; Rao, K. V.; Owens, F. J.; Sharma, R.; Ahuja, R.; Guillen, J. M. O.; Johansson, B.; Gehring, G. A. Ferromagnetism Above Room Temperature in Bulk and Transparent Thin Films of Mn-Doped ZnO. *Nat. Mater.* **2003**, *2*, 673−677.
(20) Matsumoto, Y.; Murakami, M.; Shono, T.; Hasegawa, T.; Fukumura, T.; Kawasaki, M.; Ahmet, P.; Chikyow, T.; Koshihara, S.; Koinuma, H. Room-Temperature Ferromagnetism in Transparent Transition Metal-Doped Titanium Dioxide. *Science* **2001**, *291*, 854−856.
(21) Xing, G. Z.; Yi, J. B.; Wang, D. D.; Liao, L.; Yu, T.; Shen, Z. X.; Huan, C. H. A.; Sum, T. C.; Ding, J.; Wu, T. Strong Correlation between Ferromagnetism and Oxygen Deficiency in Cr-Doped $In_2O_{3-\delta}$ Nanostructures. *Phys. Rev. B* **2009**, *79*, 174406-1−174406-9.
(22) Sundaresan, A.; Bhargavi, R.; Rangarajan, N.; Siddesh, U.; Rao, C. N. R. Ferromagnetism as a Universal Feature of Nanoparticles of the Otherwise Nonmagnetic Oxides. *Phys. Rev. B* **2006**, *74*, 161306-1−16106-4.
(23) Venkatesan, M.; Fitzgerald, C. B.; Coey, J. M. D. Unexpected Magnetism in a Dielectric Oxide. *Nature* **2004**, *430*, 630−630.
(24) Coey, J. M. D.; Venkatesan, M.; Stamenov, P.; Fitzgerald, C. B.; Dorneles, L. S. Magnetism in Hafnium Dioxide. *Phys. Rev. B* **2005**, *72*, 024450-1−024450-6.
(25) Coey, J. M. D.; Venkatesan, M.; Fitzgerald, C. B. Donor Impurity Band Exchange in Dilute Ferromagnetic Oxides. *Nat. Mater.* **2005**, *4*, 173−179.
(26) Thurber, A.; Reddy, K. M.; Shutthanandan, V.; Engelhard, M. H.; Wang, C.; Hays, J.; Punnoose, A. Ferromagnetism in Chemically Synthesized CeO_2 Nanoparticles by Ni Doping. *Phys. Rev. B* **2007**, *76*, 165206-1−165206-8.
(27) Vodungbo, B.; Zheng, Y.; Vidal, F.; Demaille, D.; Etgens, V. H. Room Temperature Ferromagnetism of Co Doped CeO_{2-x} Diluted Magnetic Oxide: Effect of Oxygen and Anisotropy. *Appl. Phys. Lett.* **2007**, *90*, 062510-1−062510-3.
(28) Tiwari, A.; Bhosle, V. M.; Ramachandran, S.; Sudhakar, N.; Narayan, J.; Budak, S.; Gupta, A. Ferromagnetism in Co Doped CeO_2: Observation of A Giant Magnetic Moment with A High Curie Temperature. *Appl. Phys. Lett.* **2006**, *88*, 142511-1−142511-3.
(29) Prestgard, M. C.; Siegel, G.; Ma, Q.; Tiwari, A. Magnetic Characteristics of Phase-Separated CeO_2:Co Thin Films. *Appl. Phys. Lett.* **2013**, *103*, 102409-1−102409-1-4.
(30) Ferreira, N. S.; Abraçado, L. G.; Macêdo, M. A. The Effects of Cr-Doping on the Room Temperature Ferromagnetism of Chemically Synthesized $CeO_{2-\delta}$ Nanoparticles. *Phys. B (Amsterdam, Neth.)* **2012**, *407*, 3218−3221.
(31) Slusser, P.; Kumar, D.; Tiwari, A. Unexpected Magnetic Behavior of Cu-Doped CeO_2. *Appl. Phys. Lett.* **2010**, *96*, 142506-1−142506-3.
(32) Dohčević-Mitrović, Z. D.; Paunović, N.; Radović, M.; Popović, Z. V.; Matović, B.; Cekić, B.; Ivanovski, V. Valence State Dependent Room-Temperature Ferromagnetism in Fe-Doped Ceria Nanocrystals. *Appl. Phys. Lett.* **2010**, *96*, 203104-1−203104-3.
(33) Chen, X.; Li, G.; Su, Y.; Qiu, X.; Li, L.; Zou, Z. Synthesis and Room-Temperature Ferromagnetism of CeO_2 Nanocrystals with Nonmagnetic Ca^{2+} Doping. *Nanotechnology* **2009**, *20*, 115606-1−115606-8.
(34) McBride, J. R.; Hass, K. C.; Poindexter, B. D.; Weber, W. H. Raman and X-Ray Studies of $Ce_{1-x}RE_xO_{2-y}$, where RE=La, Pr, Nd, Eu, Gd, and Tb. *J. Appl. Phys.* **1994**, *76*, 2435−2441.
(35) Adachi, G.; Imanaka, N.; Kang, Z. C. *Binary Rare Earth Oxides*; Springer: Dordrecht, The Netherlands, 2004.
(36) Paunović, N.; Dohčević-Mitrović, Z.; Scurtu, R.; Aškrabić, S.; Prekajski, M.; Matović, B.; Popović, Z. V. Suppression of Inherent Ferromagnetism in Pr-Doped CeO_2 Nanocrystals. *Nanoscale* **2012**, *4*, 5469−5476.
(37) Li, G.-R.; Qu, D.-L.; Arurault, L.; Tong, Y.-X. Hierarchically Porous Gd^{3+}-Doped CeO_2 Nanostructures for the Remarkable Enhancement of Optical and Magnetic Properties. *J. Phys. Chem. C* **2009**, *113*, 1235−1241.
(38) Schroeder, T.; Giussani, A.; Dabrowski, J.; Zaumseil, P.; Müssig, H.-J.; Seifarth, O.; Storck, P. Engineered Si Wafers: On the Role of Oxide Heterostructures as Buffers for the Integration of Alternative Semiconductors. *Phys. Status Solidi C* **2009**, *6*, 653.
(39) Niu, G.; Zoellner, M. H.; Zaumseil, P.; Pouliopoulos, A.; d'Acapito, F.; Schroeder, T.; Boscherini, F. X-ray Diffraction and Extended X-ray Absorption Fine Structure Study of Epitaxial Mixed Ternary Bixbyite $Pr_xY_{2-x}O_3$ (x=0-2) Films on Si (111). *J. Appl. Phys.* **2013**, *113*, 043504-1−043504-6.
(40) Stanek, C. R.; McClellan, K. J.; Uberuaga, B. P.; Sickafus, K. E.; Levy, M. R.; Grimes, R. W. Determining the Site Preference of Trivalent Dopants in Bixbyite Sesquioxides by Atomic-Scale Simulations. *Phys. Rev. B* **2007**, *75*, 134101-1−134101-7.
(41) Giussani, A.; Zaumseil, P.; Seifarth, O.; Storck, P.; Schroeder, T. A Novel Engineered Oxide Buffer Approach for Fully Lattice-Matched SOI Heterostructures. *New J. Phys.* **2010**, *12*, 093005-1−093005-12.
(42) Zoellner, M. H.; Dabrowski, J.; Zaumseil, P.; Giussani, A.; Schubert, M. A.; Lupina, G.; Wilkens, H.; Wollschläger, J.; Reichling, M.; Bäumer, M.; Schroeder, T. Stacking Behavior of Twin-Free Type-B Oriented CeO_2 (111) Films on Hexagonal Pr_2O_3 (0001)/Si (111) Systems. *Phys. Rev. B* **2012**, *85*, 035302-1−035302-9.
(43) Schroeder, T.; Zaumseil, P.; Weidner, G.; Wenger, C.; Dabrowski, J.; Müssig, H.-J. On the Epitaxy of Single Crystalline, Twin-Free Cubic Pr_2O_3 (111) Films on Si (111). *J. Appl. Phys.* **2006**, *99*, 014101-1−014101-9.
(44) Wilke, A.; Yang, J.-M.; Kim, J. W.; Seifarth, O.; Dietrich, B.; Giussani, A.; Zaumseil, P.; Storck, P.; Schroeder, T. Complex Interface and Growth Analysis of Single Crystalline Epi-Si (111)/Y_2O_3/Pr_2O_3/Si (111) Heterostructures: Strain Engineering by Oxide Buffer Control. *Surf. Interface Anal.* **2010**, *43*, 827−835.
(45) Li, L.; Chen, L.; Qihe, R.; Li, G. Magnetic Crossover of NiO Nanocrystals at Room Temperature. *Appl. Phys. Lett.* **2006**, *89*, 134102-1−134102-3.

(46) Niu, G.; Zaumseil, P.; Schubert, M. A.; Zoellner, M. H.; Dabrowski, J.; Schroeder, T. Lattice-matched Epitaxial Ternary $Pr_xY_{2-x}O_3$ Films on SrO-Passivated Si (001): Interface Engineering and Crystallography Tailoring. *Appl. Phys. Lett.* **2013**, *102*, 011906-1−011906-5.
(47) Watahiki, T.; Grosse, F.; Braun, W.; Kaganer, V. M.; Proessdorf, A.; Trampert, A.; Riechert, H. Epitaxial Growth and Structure of $(La_{1-x}Lu_x)_2O_3$ Alloys on Si (111). *Appl. Phys. Lett.* **2010**, *97*, 031911-1−031911-3.
(48) Vegard, L. Die Konstitution der Mischkristalle und die Raumfüllung der Atome. *Z. Phys.* **1921**, *5*, 17−26.
(49) Zoellner, M. H.; Zaumseil, P.; Wilkens, H.; Gevers, S.; Wollschläger, J.; Bäumer, M.; Xie, Y.-H.; Niu, G.; Schroeder, T. Stoichiometry-Structure Correlation of Epitaxial $Ce_{1-x}Pr_xO_{2-d}$ (x=0-1) Thin Films on Si (111). *J. Cryst. Growth* **2012**, *355*, 159−165.
(50) Pfau, A.; Schierbaum, K. D. The Electronic Structure of Stoichiometric and Reduced CeO_2 Surfaces: An XPS, UPS and HREELS Study. *Surf. Sci.* **1994**, *321*, 71−80.
(51) Spanier, J. E.; Robinson, R. D.; Zhang, F.; Chan, S.-W.; Herman, I. P. Size-Dependent Properties of CeO_{2-y} Nanoparticles as Studied by Raman Scattering. *Phys. Rev. B* **2001**, *64*, 245407-1−245407-8.
(52) Zhang, J.; Ju, X.; Wu, Z. Y.; Liu, T.; Hu, T. D.; Xie, Y. N.; Zhang, Z. L. Structural Characteristics of Cerium Oxide Nanocrystals Prepared by the Microemulsion Method. *Chem. Mater.* **2001**, *13*, 4192−4197.
(53) Zhang, F.; Wang, P.; Koberstein, J.; Khalid, S.; Chan, S.-W. Cerium Oxidation State in Ceria Nanoparticles Studied with X-Ray Photoelectron Spectroscopy and Absorption Near Edge Spectroscopy. *Surf. Sci.* **2004**, *563*, 74−82.
(54) Tsunekawa, S.; Fukuda, T.; Kasuya, A. X-Ray Photoelectron Spectroscopy of Monodisperse CeO_{2-x} Nanoparticles. *Surf. Sci.* **2000**, *457*, L437−L440.
(55) Ogasawara, H.; Kotani, A.; Potze, R.; Sawatzky, G. A.; Thole, B. T. Praseodymium 3d- and 4d-Core Photoemission Spectra of Pr_2O_3. *Phys. Rev. B* **1991**, *44*, 5465−5469.
(56) Schaefer, A.; Gevers, S.; Zielasek, V.; Schroeder, T.; Falta, J.; Wollschläger, J.; Bäumer, M. Photoemission Study of Praseodymia in Its Highest Oxidation State: The Necessity of in-Situ Plasma Treatment. *J. Chem. Phys.* **2011**, *134*, 054701-1−054701-7.
(57) Allahgholi, A. Untersuchung Von CeO_x-, PrO_x- und $Ce_xPr_{1-x}O_{2-\delta}$-Filmen auf Si (111) Mittels Hochenergetischer Röntgen-Photoelektronenspektroskopie; Universität Bremen: Bremen, Germany, 2013.
(58) Pan, T.-M.; Yu, T.-Y. Comparison of the Structural Properties and Electrical Characteristics of Pr_2O_3, Nd_2O_3 and Er_2O_3 Charge Trapping Layer Memories. *Semicond. Sci. Technol.* **2009**, *24*, 095022-1−095022-8.
(59) Jeon, S.; Hwang, H. Effect of Hygroscopic Nature on the Electrical Characteristics of Lanthanide Oxides (Pr_2O_3, Sm_2O_3, Gd_2O_3, and Dy_2O_3). *J. Appl. Phys.* **2003**, *93*, 6393−6395.
(60) Seifarth, O.; Schubert, M. A.; Giussani, A.; Klenov, D. O.; Schmeisser, D.; Schroeder, T. Single Crystalline $Pr_{2-x}Y_xO_3$ (x=0−2) Dielectrics on Si with Tailored Electronic and Crystallographic Structure. *J. Appl. Phys.* **2010**, *108*, 103179-1−103179-4.
(61) Tsunekawa, S.; Sivamohan, R.; Ito, S.; Kasuya, A.; Fukuda, T. Structural Study on Monosize CeO_{2-x} Nano-Particles. *Nanostruct. Mater.* **1999**, *11*, 141−147.
(62) Fernandes, V.; Schio, P.; Oliveira, A. J. A. d.; Ortiz, W. A.; Fichtner, P.; Amaral, L.; Graff, I. L.; Varalda, J.; Mattoso, N.; Schreiner, W. H.; Mosca, D. H. Ferromagnetism Induced by Oxygen and Cerium Vacancies Above the Percolation Limit in CeO_2. *J. Phys.: Condens. Matter* **2010**, *22*, 216004-1−216004-8.
(63) Soldatov, A. V.; Ivanchenko, T. S.; Longa, S. D.; Kotani, A.; Iwamoto, Y.; Bianconi, A. Crystal-Structure Effects in the Ce L3-Edge X-Ray Absorption Spectrum of CeO_2: Multiple-Scattering Resonances and Many-Body Final States. *Phys. Rev. B* **1994**, *50*, 5074−5080.
(64) Yamazaki, S.; Matsui, T.; Ohashi, T.; Arita, Y. Defect Structures in Doped CeO_2 Studied by Using XAFS Spectrometry. *Solid State Ionics* **2000**, *136*−*137*, 913−920.
(65) Pu, Z.-Y.; Lu, J.-Q.; Luo, M.-F.; Xie, Y.-L. Study of Oxygen Vacancies in $Ce_{0.9}Pr_{0.1}O_{2-y}$ Solid Solution by in Situ X-ray Diffraction and in Situ Raman Spectroscopy. *J. Phys. Chem. C* **2007**, *111*, 18695−18702.
(66) Wolf, I. D. Micro-Raman Spectroscopy to Study Local Mechanical Stress in Silicon Integrated Circuits. *Semicond. Sci. Technol.* **1996**, *11*, 139−154.
(67) Weber, W. H.; Hass, K. C.; McBride, J. R. Raman Study of CeO_2: Second-Order Scattering, Lattice Dynamics, and Particle-Size Effects. *Phys. Rev. B* **1993**, *48*, 178−185.
(68) Nakajima, A.; Yoshihara, A.; Ishigame, M. Defect-Induced Raman Spectra in Doped CeO_2. *Phys. Rev. B* **1994**, *50*, 13297−13307.
(69) Wong, H.; Yang, B. L.; Dong, S.; Iwai, H.; Kakushima, K.; Ahmet, P. Current Conduction and Stability of CeO_2/La_2O_3 Stacked Gate Dielectric. *Appl. Phys. Lett.* **2012**, *101*, 233507-1−233507-3.
(70) Li, L.; Chen, F.; Lu, J.-Q.; Luo, M.-F. Study of Defect Sites in $Ce_{1-x}M_xO_{2-\delta}$ (x = 0.2) Solid Solutions Using Raman Spectroscopy. *J. Phys. Chem. A* **2011**, *115*, 7972−7977.
(71) Małecka, M. A.; Kępiński, L.; Mišta, W. Structure Evolution of Nanocrystalline CeO_2 and $CeLnO_x$ Mixed Oxides (Ln = Pr, Tb, Lu) in O_2 and H_2 Atmosphere and Their Catalytic Activity in Soot Combustion. *Appl. Catal., B* **2007**, *74*, 290−298.
(72) Spanier, J. E.; Robinson, R. D.; Zhang, F.; Chan, S.-W.; Herman, I. P. Size-Dependent Properties of CeO_{2-y} Nanoparticles as Studied by Raman Scattering. *Phys. Rev. B* **2001**, *64*, 245407.
(73) Dohčević-Mitrović, Z. D.; Radović, M.; Šćepanović, M.; Grujić-Brojčin, M.; Popović, Z. V.; Matović, B.; Bošković, S. Temperature-Dependent Raman Study of $Ce_{0.75}Nd_{0.25}O_{2-y}$ Nanocrystals. *Appl. Phys. Lett.* **2007**, *91*, 203118-1−203118-3.
(74) Tang, Y.; Zhang, H.; Cui, L.; Ouyang, C.; Shi, S.; Tang, W.; Li, H.; Lee, J.-S.; Chen, L. First-Principles Investigation on Redox Properties of M-Doped CeO_2 (M=Mn, Pr, Sn, Zr). *Phys. Rev. B* **2010**, *82*, 125104-1−125104-9.
(75) Abraham, D. W.; Frank, M. M.; Guha, S. Absence of Magnetism in Hafnium Oxide Films. *Appl. Phys. Lett.* **2005**, *87*, 252502-1−22502-3.
(76) Shah, L. R.; Ali, B.; Zhu, H.; Wang, W. G.; Song, Y. Q.; Zhang, H. W.; Shah, S. I.; Xiao, J. Q. Detailed Study on the Role of Oxygen Vacancies in Structural, Magnetic and Transport Behavior of Magnetic Insulator: Co−CeO_2. *J. Phys.: Condens. Matter* **2009**, *21*, 486004-1−486004-9.
(77) Shah, L. R.; Wang, W.; Zhu, H.; Ali, B.; Song, Y. Q.; Zhang, H. W.; Shah, S. I.; Xiao, J. Q. Role of Dopant, Defect, and Host Oxide in the Observed Room Temperature Ferromagnetism: Co−ZnO Versus Co−CeO_2. *J. Appl. Phys.* **2009**, *105*, 07C515-1−07C515-3.
(78) Liu, Y.; Lockman, Z.; Aziz, A.; MacManus-Driscoll, J. Size Dependent Ferromagnetism in Cerium Oxide (CeO_2) Nanostructures Independent of Oxygen Vacancies. *J. Phys.: Condens. Matter* **2008**, *20*, 165201-1−165201-5.
(79) Kern, S. Magnetic Susceptibility of Praseodymium Oxides. *J. Chem. Phys.* **1964**, *40*, 208−212.
(80) Taniguchi, T.; Watanabe, T.; Sugiyama, N.; Subramani, A. K.; Wagata, H.; Matsushita, N.; Yoshimura, M. Identifying Defects in Ceria-based Nanocrystals by UV Resonance Raman Spectroscopy. *J. Phys. Chem. C* **2009**, *113*, 19789−19793.